Dynamics of Atmospheres and Oceans 103 (2023) 101372

Contents lists available at ScienceDirect

Dynamics of Atmospheres and Oceans

journal homepage: www.elsevier.com/locate/dynatmoce

How and what turbulent are deep Mariana Trench waters?

Hans van Haren

Royal Netherlands Institute for Sea Research (NIOZ), P.O. Box 59, 1790 AB Den Burg, the Netherlands

ARTICLE INFO

Keywords:
Challenger Deep
Long-term mooring
Sensitive temperature measurements
Convective turbulent intrusions
Internal wave driven turbulence
Direct bottom-effect of tropical storm

ABSTRACT

To study potentially turbulent water motions near the deepest point on Earth in the Challenger Deep of the Mariana Trench, a 588-m long string equipped with specially designed sensitive temperature sensors was moored for nearly three years. Detailed analysis of one year of good data distinguishes ubiquitous internal tidal waves and hundreds of meters slanted convection turbulent spurs due to internal waves' breaking from above. The spurs, or intrusions of anomalous waters, can occur on a tidal periodicity. Some tidal wave breaking including 100-m tall turbulent overturns reaching the trench floor is associated with warm waters that push from above, and of which the largest occurred during the passing of a tropical storm. The various turbulence types prevent the hadal, below 6000 m, waters from being stagnant, which is an important necessity for deep-trench life.

1. Introduction

As marine life including microbial activity have been found more active in deep trenches than in surrounding deep-ocean waters (Glud et al., 2013), sufficient supply of nutrients and energy are expected in the 'hadal' zones, i.e. waters deeper than 6000 m, of the ocean. Transport and redistribution of such supply require small-scale turbulence rather than smooth laminar flows. This was already noticed in the 1950's (Bogorov and Kreps, 1958). It led to the negative advice of burying hazardous waste in deep trenches and to the consideration of potential importance of turbulent convection by general geothermal heating (Tareev, 1959). While marine species have been observed at such great depths (Jamieson, 2015; Gallo et al., 2015; Nunoura et al., 2015), establishment and quantification of the relevant turbulent processes have been very limited in deep trenches. Logistical problems including the effects of large ambient pressure are a major obstacle for deep-trench observations.

As the ocean is predominantly heated from above by the sun, and warm waters are less dense than cold waters, the result is a generally stable vertical density stratification. Whilst solar radiation penetration reaches only a few hundred meters below the ocean surface, heat and stratification reach all the way down to trench floors. This deep reaching of relatively warm water is mainly due to the mechanical work of downward turbulent diffusion. The dominant turbulence generator is the breaking of internal waves (e.g., Eriksen, 1982; Thorpe, 1987; Sarkar and Scotti, 2017), either shear-driven in the ocean interior or more buoyancy- (convection-)driven near sloping seafloor topography. The deeper one gets into the ocean, the generally weaker the stratification while turbulence may increase over (sloping) topography. With increasing depth, freely propagating internal waves become slower and less energetic. Their frequency traditionally ranges between inertial frequency $f = 2\Omega\sin\varphi$, the vertical Coriolis parameter of Earth rotational vector $\mathbf{\Omega}$ at latitude φ, and buoyancy frequency N of vertical density (ρ) stratification $d\rho/dz \propto N^2$. In deep trenches, stratification is extremely weak but non-zero as $N = O(f)$.

Under such weakly stratified conditions two important physical processes are modified in general, compared to well-stratified

E-mail address: hans.van.haren@nioz.nl.

https://doi.org/10.1016/j.dynatmoce.2023.101372
Received 24 February 2023; Received in revised form 27 April 2023; Accepted 22 May 2023
Available online 1 June 2023

conditions N > > f. First, in weakly stratified waters of about N = f the range for freely propagating inertio-gravity waves (IGW) is no longer [f, N] as in N > > f, but modifies to $[\sigma_{min}, \sigma_{max}] = [0.6f, 1.7N]$. The above IGW-limits are computed as $[\sigma_{min}, \sigma_{max}] = 1/\sqrt{2}\bullet[(A-B)^{1/2}, (A+B)^{1/2}]$ where $A = N^2 + f^2 + f_s^2$ and $B = (A^2-(2fN)^2)^{1/2}$, with $f_s = f_h \sin\alpha$, f_h the horizontal Coriolis parameter and α the angle north of east, which results in limits below f and above N, respectively (e.g., LeBlond and Mysak, 1978). The effect of the inclusion of the non-traditional f_h is to divert near-inertial waves from near-horizontal propagation in N >> f to more vertically, in the direction of **Ω**, which is at a large angle approaching 90° to gravity in tropical waters. Instead of being near-circular as in N >> f, near-inertial horizontal motions become more elliptic in weak stratification, and a non-zero vertical current component is observed together with non-zero isopycnal excursions.

Second, the weaker stratification leads to a weaker restoring force for IGW, but also less restriction for turbulent overturns that can grow up to 100 m tall. In the deep ocean, such large but slow turbulence still distributes heat from above, in competition with convective geothermal heating from below. Although trenches are near volcanic arcs, they are characterized by low geothermal heatflows of about 25% (25 mW m^{-2}) of general ocean-floor values (Uyeda and Horai, 1979) due to the relatively thick crust of subduction zones (Uyeda, 1984). Such reduced heat-flow may nevertheless generate convection turbulence, which may be detectable in very weakly stratified waters. In such waters, convection plumes, lasting long enough compared to the time-scale of f, may divert from the direction of gravity to that of the Earth rotational vector under the action of f_h (e.g., Straneo et al., 2002; Sheremet, 2004; Wirth and Barnier, 2006). Unknown are the different contributions from geothermal heating, horizontal flow advection, internal tides and near-inertial IGW and shear to turbulence near trench floors.

In order to measure above modified processes one needs sensitive instrumentation. Besides a few short-term, mostly cable-lowered observations (e.g., Taira et al., 2005; van Haren et al., 2017), the only moored and hourly sampled current measurements so far near the deepest point on Earth, the floor of the Challenger Deep in the Mariana Trench, showed typical amplitudes of 0.02 m s^{-1} with a dominant semidiurnal tidal periodicity (Taira et al., 2004). Although Taira et al. (2004) did not provide spectral information, they mentioned sub-peaks at diurnal and inertial frequencies. In the West-Pacific, surface tides are mixed with roughly equal contributions at diurnal and semidiurnal frequencies (Gerkema, 2019). The observed tidal currents may be related to internal tides, whether propagating from local or remote sources (Jayne and St. Laurent, 2001; Morozov and Velarde, 2008). However, turbulence could not be calculated from these moored observations.

Compared to trenches, in a similarly low-stratification environment of deep Lake Baikal, observations by Ravens et al. (2000) using a shipborne microstructure profiler indicated a vertical mean buoyancy frequency N = 2 cpd (short for cycles per day), mean dissipation rates $\varepsilon = O(10^{-10})$ m^2 s^{-3} and mean vertical turbulent diffusivities $K_z = 1–9 \times 10^{-3}$ m^2 s^{-1}. These values compare well with values from shipborne CTD-observations from the Challenger Deep, Mariana Trench (van Haren et al., 2017; 2021). Near the CTD-site, a 7-km long instrumented line with high-resolution temperature (T-)sensors was moored. Preliminary results were reported from a short 6-day period when the mooring did not move, confirming such above turbulence dissipation rate values near the trench floor and which were hundred times larger than some 4.5 km higher up (van Haren, 2020).

In this paper, an elaborate sequel of the preliminary results is presented for near trench floor T-sensors after considerable post-processing, first of shipborne CTD-data that are necessary for referencing and computation of turbulence values (van Haren et al., 2021), and subsequently of the moored T-sensor data themselves (van Haren, 2022).

2. Methods

Hadal-zone internal-wave induced turbulence is studied using 295 high-resolution T-sensors that are specifically rated to withstand a pressure of 1.4×10^4 dbar (1 dbar = 10^4 Pa). The stand-alone sensors are moored at 11° 19.59′ N, 142° 11.25′ E, and 10,910 m water depth in the Challenger Deep, Mariana Trench, close to the deepest point on Earth (van Haren et al., 2017), between November 2016 and November 2019. The local planetary inertial period is $T_f = 2\pi/f = 2.54$ days. The 7-km long mooring consisted of flotation providing 2.9-kN net buoyancy at its top 4 km below the ocean surface, more than 6 km of slightly buoyant 0.006-m diameter Dyneema rope as a strength member, and two acoustic releases at 6 m above the anchor-weight. Two sections of instrumentation were in the mooring line: One around 6 km consisting of a single-point Nortek AquaDopp acoustic current meter (CM), and one between 595 and 7 m above the trench floor consisting of the 295 T-sensors. The current meter sampled at a rate of once per 600 s, the T-sensors at once per 2 s

All NIOZ4 T-sensors (thermistors developed by Royal Netherlands Institute for Sea Research; van Haren, 2018) were attached at 2.0 m intervals to a 0.0063 m diameter nylon-coated steel cable. Their clocks were synchronized to within 0.02 s via induction every 4 h. The sensors' precision, or relative accuracy governed by instrumental noise and short-term drift (Huber, 2018), is less than 0.0005 °C; the noise level less than 0.0001 °C and, after aging, drift maximum 0.001 °C mo^{-1}usually for the first month after deployment and typically smaller by a factor of 10 later on. Electronic (noise, battery) problems caused failure of about 20% of the sensors after one year and their data were linearly interpolated between neighboring sensors. The extremely weak stratification with N ≈ 2 f (van Haren et al., 2021) requires a second order pressure correction (van Haren, 2022), besides standard noise and electronic drift correction via polynomial smoothing of short-period average profiles during post-processing (van Haren, 2018). The second order pressure correction covers the effects of large-scale surface waves, such as tides, and mooring motion. A vertical variation of 1 m against the local adiabatic lapse rate of -10^{-4} °C m^{-1} shows as 200-m tall artificial internal waves that appear uniform without phase variation over the sensors' vertical range. Mooring motion up to vertical variations of $|dz| = 10$ m as measured by the pressure sensor of the CM at z = −6.1 km are successfully corrected after fine-tuning the post-processing per six-day periods. As a result, about 85% of year-long good T-data can be analyzed in detail for internal wave turbulence to a precision < 0.0002 °C for originally sampled unfiltered data over short 6-day periods (van Haren, 2022).

For reference, shipborne SeaBird 911 Conductivity Temperature Depth CTD-profiles were obtained at about 1 km from the mooring site. One profile came to 50 m from the trench floor (van Haren et al., 2021). After correction using water-sample data, the CTD-data are used to reference the moored T-sensor data in absolute value. The CTD-data are also used to establish a consistent temperature-density (variations) relationship of $\alpha\delta\Theta = \delta\sigma_{11}$, $\alpha = -0.55 \pm 0.03$ kg m^{-3} °C^{-1}, which implicitly includes salinity contributions to density variations. This relationship is used for quantification of turbulence values from the moored T-sensor data. The error in α is partially attributable to (small) salinity effects. Here, σ_{11} represents density anomaly referenced to 1.1×10^4 dbar. All analyses are performed after transferring temperature into dynamically correct Conservative (~potential) Temperature (Θ) using the Gibbs-Sea-Water-software (IOC, SCOR, IAPSO, 2010) and using constant-in-time Absolute Salinity values from CTD-data. Potential errors due to varying salinity by $\pm 10^{-4}$ g kg^{-1}, as observed over the entire T-sensor range, yield an error of $\pm 2 \times 10^{-6}$ °C in Θ, which is below detection limit of the moored T-sensors.

From the moored T-sensor data, turbulence dissipation rate $\varepsilon = c_1^2 d^2 N_s^3$ is calculated, for each time-step t, using the method (Thorpe, 1977) of reordering original potentially unstable vertical density, and thus Conservative Temperature, profiles $\sigma_{11}(z)$ into stable monotonic profiles $\sigma_{11}(z_s)$. Here, $d = \min(|z\text{-}z_s|)\cdot\mathrm{sgn}(z\text{-}z_s)$ denotes the displacements between unordered (original) and reordered σ_{11}-profiles. N_s denotes the local 2-m small-scale buoyancy frequency computed from the reordered stable profiles. Tests are applied to disregard apparent displacements which are associated with instrumental noise and post-calibration errors (Galbraith and Kelley, 1996). Such a test-threshold is very low for original NIOZ T-sensor data, with noise level <0.0001 °C. This noise level is reduced to <0.000005 °C for corrected and low-pass filtered data considered in Section 3. As a result, the expected detectable overturn size is <2.5 m, which is in accordance with the vertical interval between sensors. Precision of such filtered data is <0.00002 °C after extended post-processing, except for the first month after deployment.

Root-mean-square-values d_{rms} of displacements are not determined over individual overturns, as in Dillon (1982), but over parts of 588-m vertical intervals that exceed the largest overturn intervals. This is because individual overturns cannot be easily distinguished, as they occur at various scales with small ones overprinting larger overturns, as one expects from turbulence, and because some exceed the range of T-sensors. We use standard constant values of $c_1 = 0.8 = L_O/d_{rms}$ for the Ozmidov/overturn scale factor (Dillon, 1982), which is the mean value in an at least one order of magnitude wide distribution of many realizations of different turbulence type values established from microstructure profiler data. This is the most commonly used parameterization for oceanographic data after 'sufficient averaging' to achieve statistical stationarity (Gregg et al., 2018).

Sufficient averaging is feasible for the moored T-sensor data, both in the vertical and in time. Six-day mean values contain information from a sufficient mix of samples from shear- and convection-driven turbulence to warrant the above c_1 in the high Reynolds number environment of the deep ocean (Mater et al., 2015; Portwood et al., 2019). Comparison between calculated turbulence values using microstructure-profiler shear measurements and overturn scales with above constant led to 'consistent results' that support the use of such a constant value (Nash et al., 2007).

Vertical eddy diffusivity $K_z = m_1 c_1^2 d^2 N_s$ and $m_1 = 0.2$ is used for mean mixing efficiency coefficient (Osborn, 1980; Oakey, 1982). This value for m_1 has also been found (to within error) using microstructure profiler in the weakly stratified waters of Lake Baikal (Ravens et al., 2000).

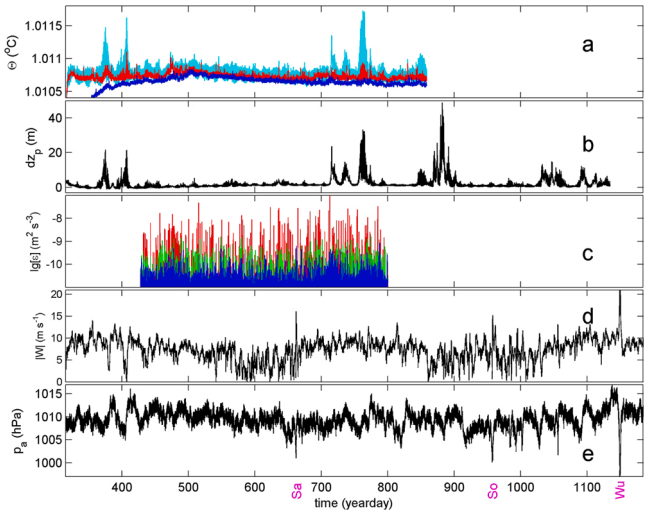

Fig. 1. Nearly 3 years of time series of environmental and deep Mariana Trench data. Yeardays (UTC) in 2017 are +365, in 2018 + 730 and in 2019 + 1005. (a) Temperature from moored T-sensors near z = −10.3 km (in cyan uncorrected; in red generally corrected for mooring motions and tides) and z = −10.9 km (in blue detrended and mooring-motion corrected), low-pass filtered (lpf) for noise reduction with cut-off at 30 cpd (short for cycles per day). (b) Pressure (converted to relative vertical coordinates) measured at z = −6.1 km. (c) Logarithm of 100-m vertically averaged dissipation rates from moored T-sensor data around z = −10.35 km (red), − 10.6 km (green) and − 10.85 km (blue). (d) Local wind speed from model run by Meteoblue. (e) Local air pressure from Meteoblue-model. Times of approximate passage over the mooring site are indicated of tropical cyclone Wu(tip) and tropical storms Sa(ola) and So(ulik).

Mean turbulence values are calculated by arithmetically averaging ε(t, z) in the vertical […] or in time <…>, or both. Mean K_z-values are obtained by averaging flux-values first. Although Θ-data are analyzed throughout, "temperature" is used henceforth as a shorthand for Conservative Temperature.

Atmospheric data are obtained from Meteoblue, who use a mix of numerical models and observations from various national weather searvices. For the Pacific, an important Meteoblue product for atmospheric data-generation is the global numerical weather model NEMS30, see https://content.meteoblue.com/en/research-education/specifications/data-sources.

3. Observations

3.1. Year-long overview

Because the T-sensor mooring was about one year longer underwater than originally planned due to logistic problems, all instrumentation had consumed their self-contained power well before the date of recovery. A few T-sensors provided about 1.5 y of data (Fig. 1a), while CM was the only instrument delivering more than 2 y of data (Fig. 1b).

In general, deep Mariana Trench temperature does not vary by more than 0.001 °C over 1.5 y (Fig. 1a). Apart for the first two days after deployment, in which both sensors gave 0.001 °C drift (not shown), one sensor hardly showed any drift through the remainder of the record and the other, detrended in blue here, showed 0.001 °C for the subsequent first month and another 0.001 °C for the following 400 days. Most of this variation in original temperature data is artificial due to mooring motions of up to $|dz| = 20$ m as measured by the CM-pressure sensor at $z = -6.1$ km (Fig. 1b), and which corresponds to about $|dz| = 2$ m at $z = -10.6$ km halfway the deep T-sensor range. These artificial mooring motions, which generate one-sided positive Θ-variations, are due to (mainly tidal) sea-surface level variations demanding additional pressure-related corrections to original T-sensor data. Pressure variations due to mooring motions follow the yearly pattern of (northeasterly) trade winds, with larger values during increased wind speeds. Exception are the mooring motions between days 850 and 900, but by then all T-sensors stopped working. Together with instrumental drift that is relatively large for most T-sensors and the CM-pressure sensor during the first 3 months after mooring deployment, the detrended, mooring-motion corrected and low-pass filtered year-long records between days 430 and 795 demonstrate temperature variations <0.0005 °C (Fig. 1a).

All T-sensor time series are low-pass filtered with cut-off at 30 cpd using a sharp double-elliptic filter that preserves phase (Parks and Burrus, 1987). The filter cut-off is a compromise between maximum reduction of noise and passing of turbulent motions. The low-pass filtering reduces the noise level to < 0.000005 °C.

During that one year of 75–90% good T-sensor data, 100-m vertically averaged turbulence dissipation rate for three layers vary over four orders of magnitude (Fig. 1c). These temporal variations are not conclusive of potential sources or turbulence types from the 3-y data overview in Fig. 1, also not when compared with unlikely potential influencers like atmospheric wind speed (Fig. 1d) and air pressure (Fig. 1e). Such comparison has some particular interest, as it is known that large atmospheric disturbances like tropical cyclones do reach and affect 4-km deep ocean floors (Morozov and Velarde, 2008). Tropical cyclones generally occur when trade winds

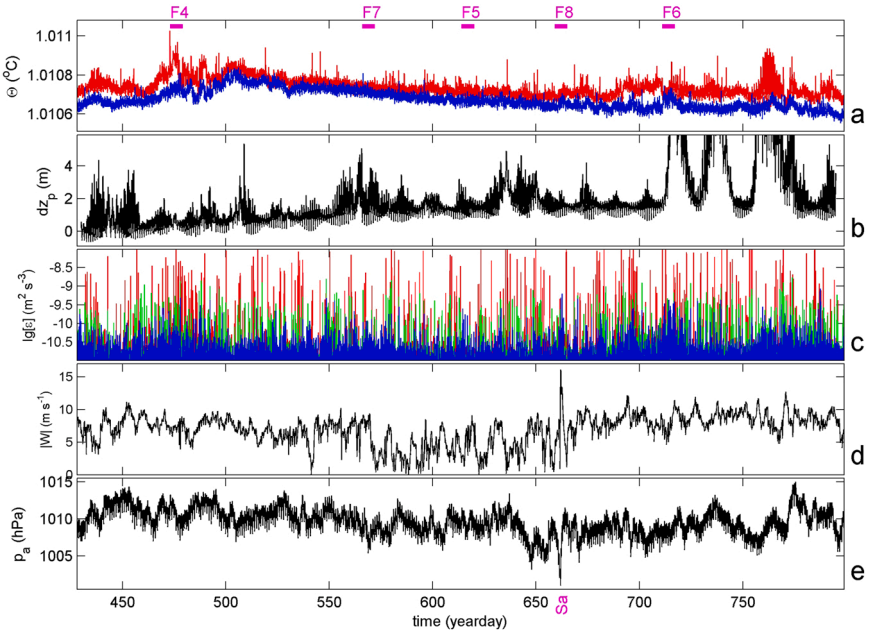

Fig. 2. As Fig. 1, but for one year of best T-sensor data. Y-axis scales are adapted for better visualization. In a., the uncorrected T-sensor data are not plotted while six-day periods of F(igures) 4–8 are indicated by purple bars.

have decreased and they are associated with increased rain-fall. Unfortunately, during the three years of underwater mooring only one tropical cyclone (Wutip) passed over the site after all T-sensors and evem the CM had stopped working. Only one tropical storm (Saola) passed overhead during the one year of good T-sensor data.

The one year data overview for the period between days 430 and 795 (Fig. 2) demonstrates no evident correspondence between temperature (Fig. 2a), pressure (Fig. 2b) and atmospheric data variations (Fig. 2d,e). Generally lower wind speeds occur between days 570 and 600, without a clear reduction in deep Mariana Trench turbulence dissipation rate (Fig. 2c). This may not be too surprising considering the >10 km great depths. Larger atmospheric variations of 10–30 day periodicity in wind speed and air pressure are also not clearly reflected in T-sensor data near the trench floor. While air-pressure (Fig. 2e) demonstrates semidiurnal tidal variations, a spring-neap cycle is not visible like in (sea-)pressure (Fig. 2b).

More detailed investigation is thus required on fine-tuned corrected moored T-sensor data over six-day periods. These periods are chosen to cover the different turbulence strengths and types, including short-scale slanted spurs, or intrusions of water, and tidal variations (for periods in time see Fig. 2a). A cold spur is short-scale upward movement of cold water and warm spur is short-scale downward movement of warm water. Their six-day length is long enough to exceed the local inertial period and short enough to properly correct for drift (van Haren, 2018). Of particular interest is turbulence reaching the trench floor with the potential to resuspend matter. Spectral information is investigated focusing on the super-buoyancy turbulence range containing either dominant shear- or convection-turbulence, or neither. One detailed investigation associates with Saola, during its one-sided passage over the mooring site (Fig. 3). The below presented five six-day periods add to the one previously analyzed (van Haren, 2020), which is a rare example when the mooring motions were negligible with <0.1 m vertical deflections at z = −10.6 km.

3.2. Six-day detailed periods

For each detailed period, 6-day and 588-m mean turbulence values are given in Table 1. The applied low-pass filter effectively removes most of instrumental white noise as will be clear from changes in spectral slope. This leaves an effective turbulence range of about one order of magnitude to be studied [$N_{s,max}$ (=3–6 cpd), filter (30 cpd)]. Here, $N_{s,max}$ represents the maximum 2-m small-scale buoyancy frequency, which is computed from reordered time series in addition to large-scale, in this case 196-m, N. Time series of turbulence dissipation rate are vertically averaged over 196 m, which provides three values over the full T-sensor range per time step: For upper (nominal vertical range $-10{,}511 \le z \le -10{,}315$ m, also referred to as "−10.4 km"), middle ($-10{,}707 \le z \le -10{,}511$ m, "−10.6 km") and lower ($-10{,}903 \le z \le -10{,}707$ m, "−10.8 km") layer. As artificial effects of tidal mooring motions cannot be

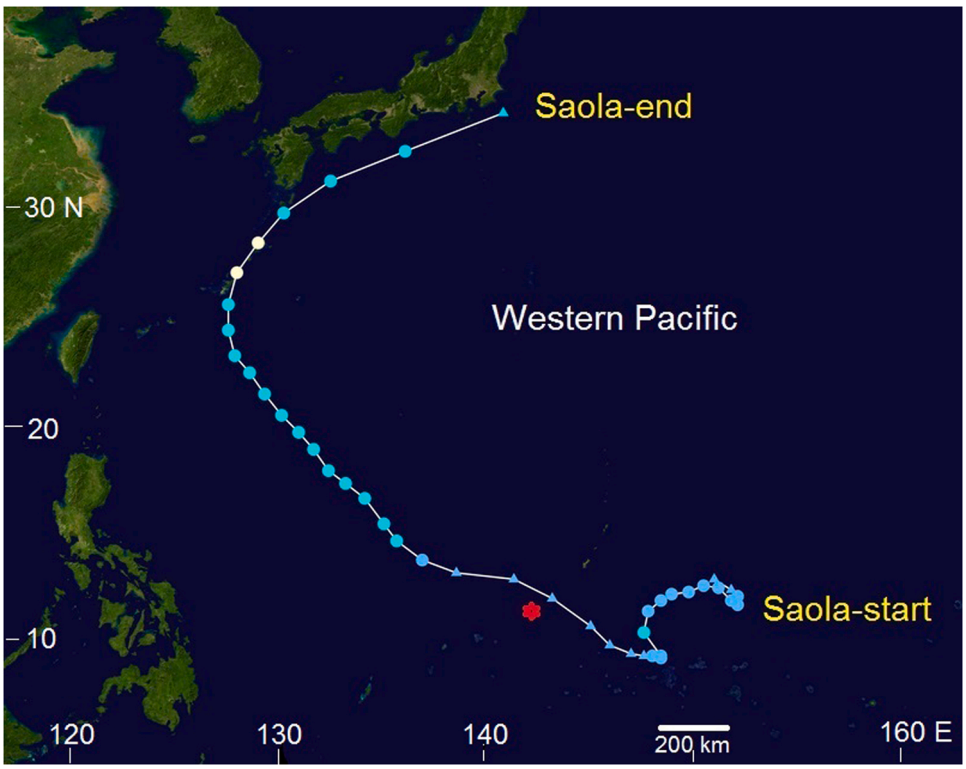

Fig. 3. Track of center of tropical storm Saola with closest passage of about 60 km North of the deep Mariana Trench mooring site (red *). Image Source: https://commons.wikimedia.org/wiki/File:Saola_2017_track.png. Saola's horizontal extent of intense winds have a diameter of at least 100 km around its center, which corresponds with general tropical storm sizes (Kueh et al., 2019).

Table 1
A glossary of deep Mariana Trench turbulence events in six-day observations. For all, 6-day and 588-m mean [$<N>$] = 0.76 ± 0.03 cpd ≈ 1.92 ± 0.07 f from CTD-profiles. The time-mean of small-scale per-profile-maximum $<N_{s,max}>$ = 1.93 ± 0.15 cpd = 4.9 ± 0.4 f ≈ M_2. In the table, $N_{s,max}$ indicates the absolute maximum of small-scale buoyancy frequencies per 6-day period.

First-day	[$<\varepsilon>$] ($m^2\ s^{-3}$)	[$<K_z>$] ($m^2\ s^{-1}$)	$N_{s,max}$ (cpd)	description
473.0	$1.4 \pm 1 \times 10^{-10}$	$5 \pm 2 \times 10^{-3}$	7.0	Strong turbulence from above
614.0	$1.3 \pm 1 \times 10^{-11}$	$7 \pm 3 \times 10^{-4}$	3.6	Weak turbulence
711.0	$1.0 \pm 0.5 \times 10^{-10}$	$2.1 \pm 1 \times 10^{-3}$	7.2	Tidal turbulence at floor
566.0	$1.9 \pm 1 \times 10^{-11}$	$1.0 \pm 0.5 \times 10^{-3}$	4.7	Spurs reaching floor
659.0	$3 \pm 2 \times 10^{-11}$	$1.1 \pm 0.5 \times 10^{-3}$	6.5	Floor tidal turbulence Saola

completely removed from the internal wave band in the temperature records (van Haren, 2022), although some fine-tuning is done here, the focus will be on the turbulence range. It is noted that the removal of (tidal) mooring motions does not affect turbulence levels, it only spoils visual imaging.

3.2.1. Six-day period 473: strong turbulence from above

During a period of weakening trade winds, the T-sensor data reveal ubiquitous internal wave and turbulence activity in the lower 600 m above the floor of the Challenger Deep (Fig. 4a). During this 6-day period mooring motions caused |dz| <1 m artificial vertical excursions at z = −6.1 km. Obvious semidiurnal isotherm variations have nearly 100-m amplitudes that vary vertically as well as in time-phase. (They are thus representing internal waves instead of vertically uniform surface wave pressure artifacts, see van Haren, 2022). A large warming of +0.0001 °C from above is seen in the upper half, between days 474.3 and 476.8, lasting about one inertial period before diurnal periods of isotherm displacement become dominant.

The semidiurnal variations steepen, deform and overturn, e.g. day 473.8, z = −10.8 km, and day 475.7, z = −10.7 km. The

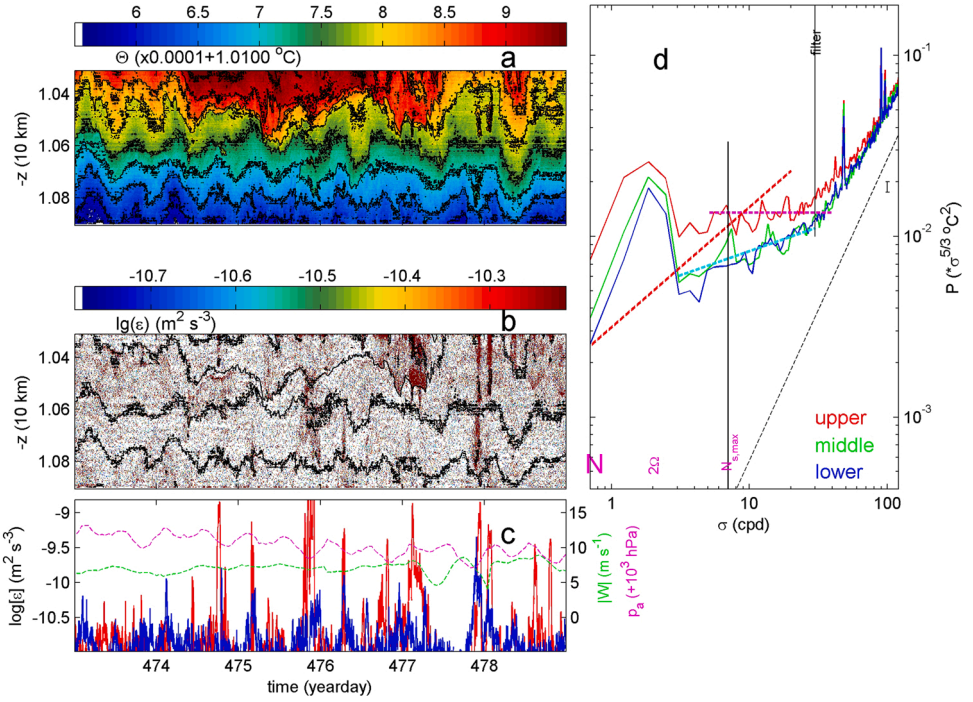

Fig. 4. Six-day detail of fine-tuned corrected moored T-sensor data, with relatively large mean (convection) turbulence values related with internal waves mainly from above overprinted with short-scale spurs (see text). (a) Time-depth series of 10-s subsampled temperature with black contours every 0.00005 °C. The trench floor is at the level of the x-axis. (b) As a., but for logarithm of non-averaged turbulence dissipation rate, with every 0.0001 °C black temperature contours from a. given for reference. (c) Logarithm of upper (red) and lower (blue) 196-m averaged turbulence dissipation rates, with wind-speed (green-dashed) and surface-air pressure (magenta-dashed) given for reference. (d) Considerably smoothed, about 300 degrees of freedom, 196-m vertically averaged unfiltered temperature variance frequency (σ) spectra. The spectra are scaled with the power law $\sigma^{-5/3}$, which reflects the turbulence inertial sub-range. In red data around z = −10.4 km, in green − 10.6 km, in blue − 10.8 km. Inertial frequency f, semidiurnal 2 Ω and mean N and maximum $N_{s,max}$ (solid vertical line) buoyancy frequencies are indicated, besides the low-pass filter cut-off (solid vertical line). Note that 2 Ω ≈ f_h ≈ 5 f ≈ σ_{max} (see text). The purple dashed line has slope 0 (log-log plot) and represents dominant shear-induced turbulence. The red dashed line has slope + 2/3 (log-log plot) and indicates internal wave (intermittency). The cyan-dashed line has slope + 4/15 and indicates dominant convection turbulence. The slanted black-dashed line slopes at + 5/3 and indicates instrumental white noise.

associated turbulence is spread vertically over up to 200 m and 1–3 h in time (Fig. 4b). In general during this 6-day period, many small turbulence activities occur, as will become clearer once the other periods are presented. Short-scale turbulent spurs reflected in positive temperature anomalies of 0.25–1 h duration extend vertically over up to 400 m. Such spurs were found abundant in the previously presented no-mooring-motion period (van Haren, 2020). Like in those data, the spurs dominate average turbulence dissipation rate data even though their duration in time is relatively small (Fig. 4c; note the logarithmic y-axis scale). While spurs sometimes occur on a semidiurnal time-scale, e.g. on day 475, their appearance is generally more erratic, especially in the upper layer of observations. Here, the spurs appear more intense with the inertial-scale warming from above.

Turbulence values in the lower layer however, seem to increase and decrease on a more regular semidiurnal and, between days 475.5 and 478.5, diurnal periodicity. This lower-range turbulence is not outstanding in the non-averaged turbulence dissipation rate plot (Fig. 4b), and extends over some 100 m above the trench floor. It seems not associated with friction of flow over the trench floor as the Ekman depth $\delta = \sqrt{(2\ A/f)} = 18$ m using turbulent diffusivity K_z from Table 1 to replace turbulent viscosity A. More likely, it is associated with internal wave breaking, some distance away from the mooring and occasionally reaching the trench floor. For reference, the 6-day period is characterized by moderate and steady wind-speeds, and (solar) semidiurnal periodic dominated air pressure (Fig. 4c).

In frequency (σ), six-day mean temperature variance spectra (scaled with $\sigma^{-5/3}$) show per layer a distinctive difference in turbulence range slopes (Fig. 4d). While the upper-layer turbulence range, with largest variance, attains a slope close to the inertial subrange slope of zero (−5/3 in an unscaled log-log plot), the deeper layers scale close to + 4/15 (−7/5 in an unscaled plot). The former slope thus points at dominant shear-induced turbulence of a passive scalar (Tennekes and Lumley, 1972; Warhaft, 2000) during the inertial-period warming. The latter slope points at dominant convection-turbulence of an active scalar (Bolgiano, 1959; Pawar and Arakeri, 2016), even though the stratification is about the same for all layers.

It is not well understood how the tidal periodicity affects the convection-turbulence near the trench floor. The relative warming by 0.0001 °C during one inertial period can be advected by slantwise convection (Straneo et al., 2002) as deep waters are stably stratified but $N \approx 2\ f < 5\ f \approx f_h = 1.96\ \Omega$ and thus well below the limit of f_h for stratification and internal waves when neutral non-linear stability is in the direction of the Earth rotational vector (van Haren, 2008). It is unclear how the stable stratification is maintained then, if not considered from an (in)stability viewpoint. This will be elaborated in Section 4 (Discussion). It is noted that $\sigma_{max} = 2.13\ \Omega$ (for $N = 2f$).

Adopting such an (in)stability viewpoint it seems easier to connect with the short-scale spurs as being '5f-spurs', which have a buoyancy difference just at the limit for instabilities in the Ω-direction. Thus, they could be generated by any instability like a breaking internal wave, but unclear are their limited durations of 0.25–1 h. The spurs fill-in the gap: Their buoyancy surplus is close to the above limit as $N_{sp} = 5f$ over the range of spurs. They come in patches of about 20-m thickness, see also the detailed Fig. 3 in van Haren (2020), in which they have a surplus of temperature of about 0.00005 °C with respect to their immediate environment, resulting in the above N_{sp}. This association with slant-wise convection and particular stratification as mean small-scale buoyancy frequency is also close to 5f

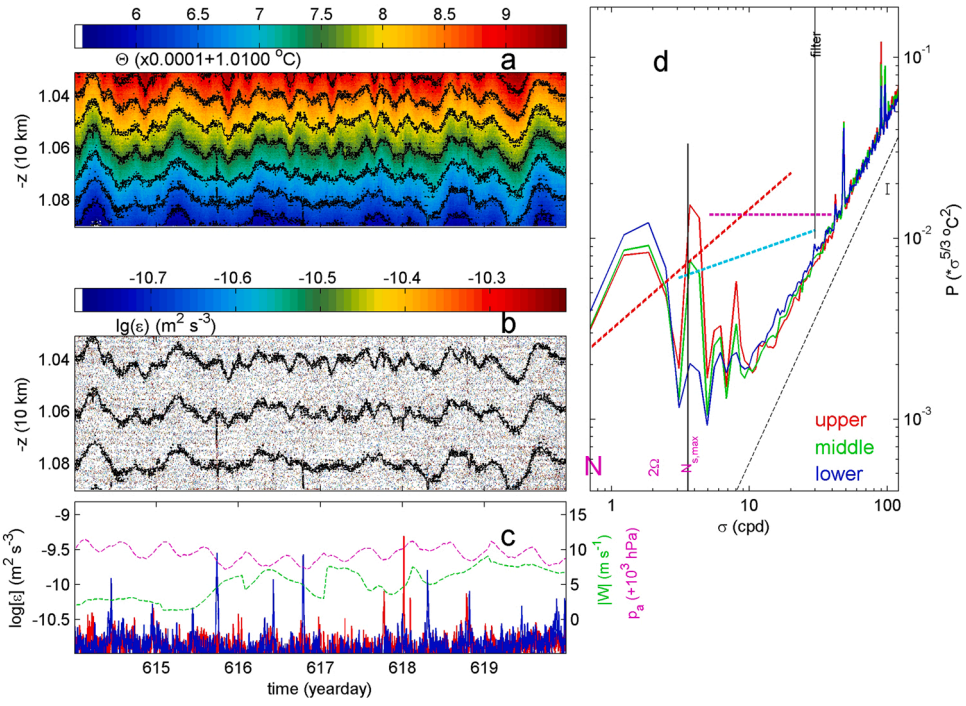

Fig. 5. As Fig. 4 with all sloping spectral lines identical for reference in d., but for a period with low turbulence except for a few short-scale spurs some of which reaching the trench floor.

(Table 1) will be further discussed in Section 4.

3.2.2. Six-day period 614: weak turbulence

The turbulence and internal waves of Fig. 4 may be better appreciated after comparison with Fig. 5, which shows tenfold weaker mean turbulence, about the weakest in the year-long record, and more pronounced small-scale internal waves near the (factor of two smaller) maximum buoyancy frequency. The isotherms in Fig. 5a,b and the colouring in Fig. 5b are less intensely varying than in Fig. 4a,b. During the period of Fig. 5, tidal mooring motions were about $|dz| = 2$ m. These observations were made during weak winds, being not an episode of trade winds, but also without passage of a tropical storm. Several short-scale spurs are observed, two of which reaching the trench floor. As before, here the weak turbulence near the trench floor shows a semidiurnal periodicity, which is less clear in the even weaker turbulence higher up. For this case, the Ekman layer height of frictional flow would be $\delta \approx 7$ m.

While the spurs in Fig. 4 seemed to associate with the larger turbulence induced or convected from above, the example of weak turbulence in Fig. 5 demonstrates spurs that relate with very small, about 0.1-d short duration solitary downward internal wave motions. It is unclear why these motions become non-linear, and they are not supported by the stratification as their 'periods' are considerable shorter than the minimum buoyancy period. Considering the conditions for slantwise convection, any instability could, of course, convect before rotation controls (Straneo et al., 2002), possibly launched by a local downward acceleration that has to overcome the reduced gravity, $|a| > 3 \times 10^{-8}$ g. Puzzling is why a downward spur appears solitary during a short passage through the mooring line (or a lowered CTD-trace), and why no upward spurs of negatively buoyant cold anomalies are observed, which makes the case different from conventional convection of alternating up- and down-going plumes as in Rayleigh-Taylor instabilities (e.g., Dalziel et al., 2008).

The spectra obviously show little temperature variance in the turbulence range, and adopt the roll-off to white noise at about 10 cpd. In the limited frequency range between this frequency and $N_{s,max}$ the base below the internal wave peaks has a slope between +4/15 and +2/3 (−1 in an unscaled log-log plot and reflecting internal wave intermittency), but variability is large.

3.2.3. Six-day period 711: tidal turbulence at trench floor

A medium-large turbulence example demonstrates dominant semidiurnal variations touching the trench floor with larger-valued spurs in the interior (Fig. 6). During the displayed 6-day episode, the mooring motion increases halfway from $|dz| < 2$ m to > 22 m at the end, at $z = -6.1$ km. Although the increase in mooring motion coincides with increase in near-bottom semidiurnal periodic turbulence, no obvious relationship is found: The entire 6-day episode demonstrates enhanced semidiurnal periodic turbulence near the trench floor (Fig. 6c).

The isotherm displacements demonstrate semidiurnal periodicity throughout, with a tendency for diurnal periodicity to dominate near the trench floor (Fig. 6a,b). In the spectra, the reduced semidiurnal but also diurnal periodicity in the lower layer near the trench

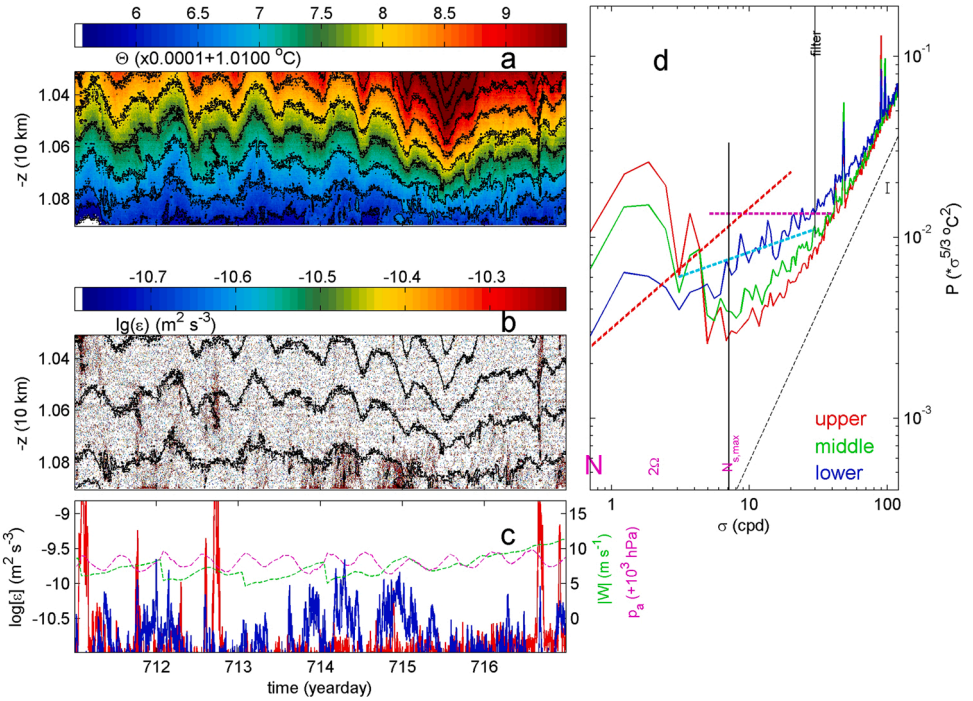

Fig. 6. As Fig. 4, but for a period with relatively large lower-layer convection turbulence reaching the trench floor when mooring motions were relatively large up to $|dz| = 22$ m at $z = -6.1$ km. Turbulence roughly has a semidiurnal periodicity, only a few short-scale spurs occur and one large Kelvin-Helmholtz instability (compared to Fig. 4).

floor are obvious compared to upper and middle layers, while temperature variance is largest near the trench floor for $\sigma > 4$ cpd (Fig. 6d). This is mostly the frequency range of turbulence, in which the spectral slopes for middle and upper layers tend to follow the intermittency slope of + 2/3, while the lower layer spectrum slopes like + 4/15 reflecting the convection-turbulence.

The near-trench floor tidal turbulence thus seems predominantly governed by convection-turbulence rather than by shear-turbulence. This is understood from the irregular lower 100 m above the trench floor in Fig. 6a, albeit with sparse up- and down-going convection plumes as has been previously observed under internal wave action in weakly stratified waters below, e.g. in fresh-water Lake Garda (van Haren and Dijkstra, 2021). Here, largest turbulence occurs during upward isotherm motions (around day 714), which is different from turbulence during downward isotherm motions as in Lake Garda and here, in weaker form, around day 716.

3.2.4. *Six-day period 566: many turbulent spurs reaching trench floor*

An example with 3-m tidal mooring motions and little turbulence is shown in Fig. 7. Its most obvious presentation is numerous turbulent short-scale spurs reaching the trench floor. Although their vertical extent and buoyancy surplus are smaller than spurs in the upper layer, the lower layer spurs are more numerous. They do not occur at a particular fixed periodicity, but a group of (even smaller) spurs is found around day 569, and possibly associate with an event of semidiurnal periodic down-going isotherms and turbulence near the trench floor.

Spectrally, the near-trench floor spurs contribute a small elevation of temperature variance compared with middle and upper layers. A small turbulence range $N_{s,max} < \sigma < 10$ cpd shows a slope close to + 4/15 before rolling to noise via the + 2/3 slope.

3.2.5. *Six-day period 659: trench floor tidal turbulence during passage of tropical storm*

An inertial-period short episode including largest semidiurnal periodic turbulence near the trench floor occurs around day 662, when tropical storm Saola passes near the mooring (Fig. 8). The 6-day period shows little mooring motion, especially during its last day, and a rather smooth image of semidiurnal-dominated internal wave motions. Precisely during the passage of Saola, as may be inferred from the sudden drop in air-pressure and increase in wind speed on day 661 lasting to day 663 (Fig. 8c), the semidiurnal periodic isotherms become rather irregular in the lower layer (Fig. 8a,b) and turbulence dissipation rate steadily increases with time (Fig. 8c). While the lower layer mean dissipation rate over 6 days equals 2.2×10^{-11} m^2 s^{-3}, it is 4.6×10^{-11} m^2 s^{-3} over days 661.5–663.0 and 1.1×10^{-10} m^2 s^{-3} over the 10-h period between days 661.4–661.8. The latter value is equivalent to a 1-h duration short-scale spur with typically 1×10^{-9} m^2 s^{-3}, as observed.

In the non-averaged turbulence dissipation rate values, a steady upward phase propagation is observed in semidiurnal periodic turbulence ‘stripes’ (Fig. 8b). Relating such phase z-t-distribution with free internal (tidal) wave propagation, this would imply downward energy propagation. If so, this may explain extra internal wave energy driving the existing linear waves to non-linear forms to the point of breaking. The direct occurrence under the passage of Saola suggests a barotropic-baroclinic coupling that governs a

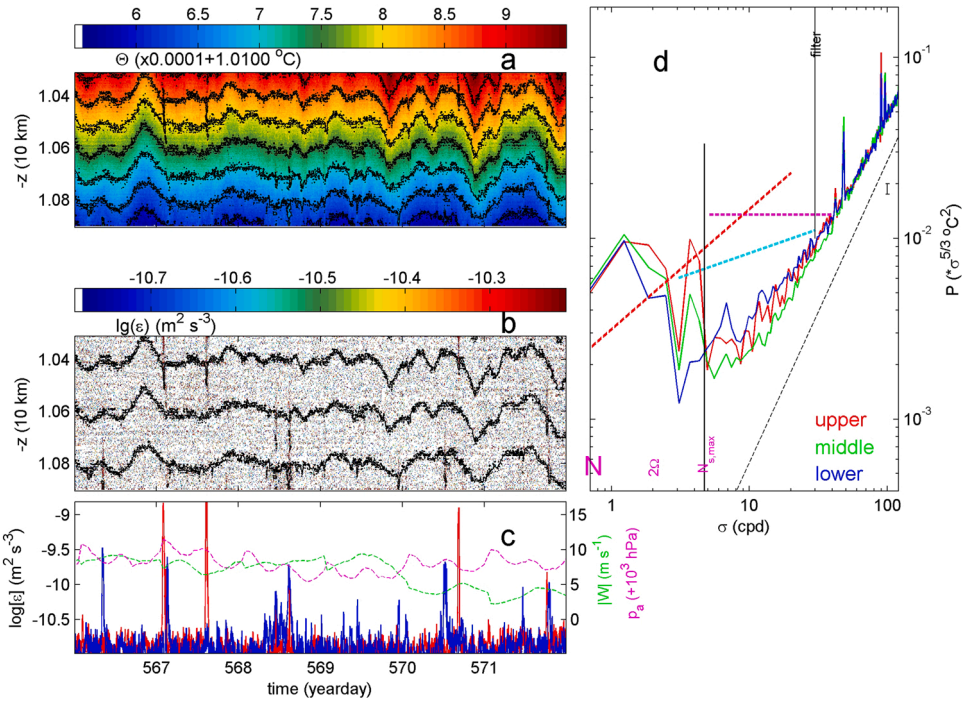

Fig. 7. As Fig. 4, but for a period with relatively low convection turbulence, dominant diurnal internal tides, and quite some short-scale spurs reaching the trench floor.

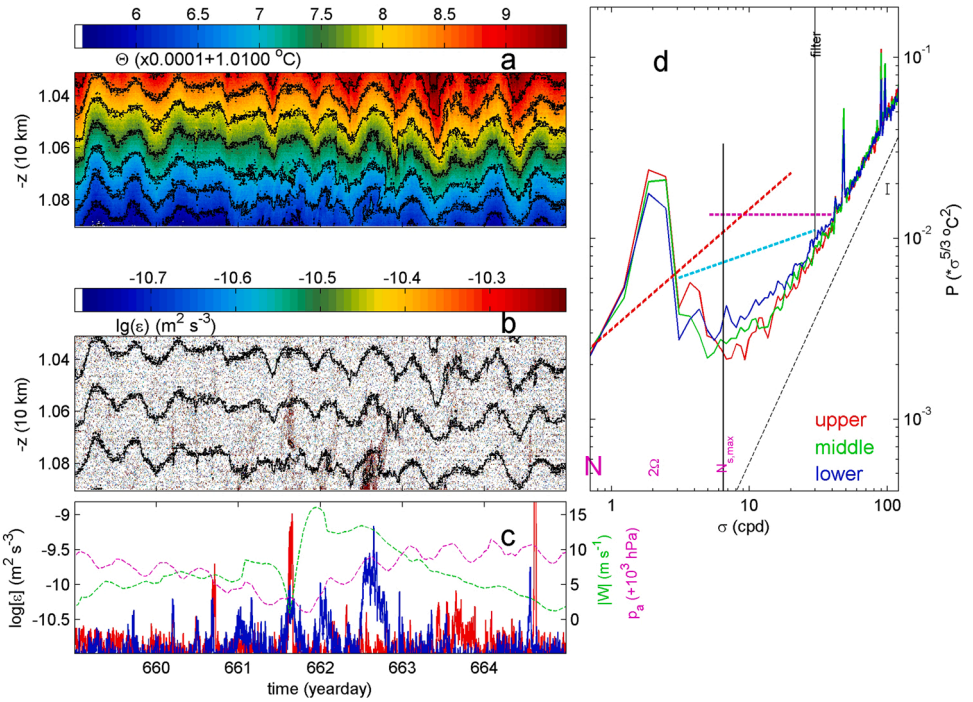

Fig. 8. As Fig. 4, but for a period with relatively largest turbulence reaching the trench floor at the time of passage of tropical storm Saola. The near-bottom turbulence is also associated with semidiurnal internal tide breaking and shows some evidence of being shear-induced.

direct response at the trench floor triggered by a tropical storm passage. Such rapid response has been suggested previously to occur in the open ocean (Shay and Elsberry, 1987; Morozov and Velarde, 2008), and inertial motions have been observed at 3000 m depth also prior to a storm passage (van Haren et al., 2020), but the present observations are from around 10.5 km in a trench.

Spectrally, the lower layer shows a small but significant increase in temperature variance over that of middle and upper layers (Fig. 8d). Beyond the semidiurnal band, the slope is almost horizontal reflecting a half-order of magnitude shear-dominated inertial subrange, with a slope of +2/3 of intermittency before roll-off in the lower layer only for $\sigma > N_{s,max}$.

A 1.5-day magnification of Fig. 8a demonstrates some details of relevant turbulence processes in the lower 330 m above the trench floor (Fig. 9). A 100-m tall spur terminating in a 25 m tall warm core is observed around day 661.6 between $-10.75 < z < -10.65$ km. The spur slants over about 2.3 h, and its core over about 1.3 h. It thus exhibits a vertical speed of about 0.012 m s^{-1}. The dominant semidiurnal motions have the same frequency as the mean of 5 f of maximum small-scale buoyancy frequencies (Table 1). Over time, the tidal motions become more non-linear and turn-over. They are superseded with motions that have

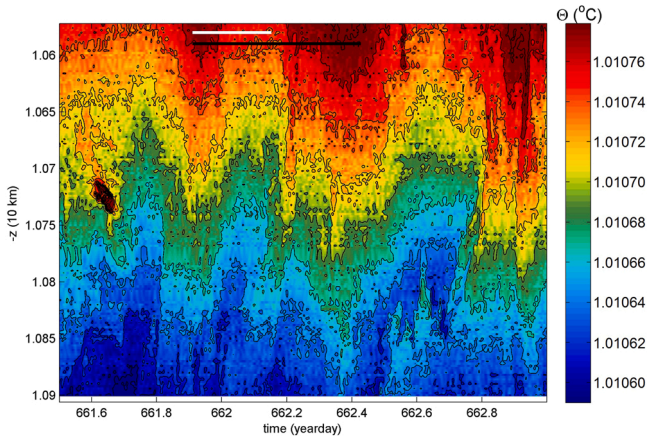

Fig. 9. Dt = 1.5-day detail of lower 330 m above the trench floor during the passage of Saola of Fig. 8a (but for 6-s sub-sampled data and 60 cpd lpf-cut-off), with shortest buoyancy period indicated by the white bar and the M_2-semidiurnal period by the black bar. Note the reduced colour-scale of only 0.00019 °C.

periodicities that are very close to that of the absolute minimum of small-scale buoyancy periods ($N_{s,max} = 10.5$ f). These small-scale motions associate with the duration of an overturn, e.g. the sequence of 4 dips to about z = −10.85 km between days 661.8 and 662.6.

4. Discussion

The various deep-trench turbulence types generate values that are one-two orders of magnitude larger than values from the more stratified waters near the trench-top, i.e. the deep-ocean surroundings (van Haren, 2020). The deep-trench values are thus three-four orders of magnitude larger than those due to molecular diffusion, which emphasizes the relative importance of turbulence for the redistribution of dissolved and suspended matter in deep-trench waters. The turbulence values may partially explain the twice larger biological oxygen consumption in deep trenches compared to the surrounding deep ocean (Glud et al., 2013). Two types of deep-trench turbulence are distinguished: Short-scale slanted convection, and (internal) tidally varying, possibly near-inertial shear-induced overturning. The two types are different in set-up and in effect on matter resuspension and redistribution.

4.1. Short-scale slanted convection

The investigation of short-scale turbulence spurs provide some refining of first results from deep trench mooring data reported in van Haren (2020). Confirmed are the duration of 0.5–1 h and value of 0.0001°C of the warm (and fresh, van Haren et al., 2021) anomalies, in the moored T-sensor data as well as in shipborne CTD-data. Also confirmed are the vertical sizes of 10–40 m of small patches which organize in 100–300 m tall ones that are slanted to the vertical. The small patches are also slanted to the vertical at a wide variety of angles, with aspect ratios between about 0.2–1.2 (van Haren, 2020). If guided by slantwise convection (Straneo et al., 2002), the high aspect ratios > 0.2 may associate with background (small-scale) shear-flow. The 0.2 aspect ratio associates with the direction of the Earth rotational vector at the tropical latitude of the mooring. It may thus reflect planetary slantwise convection due to the effects of the horizontal component of the Coriolis force (Straneo et al., 2002; Sheremet, 2004).

From the perspective of (in)stability analysis involving a balance between destabilizing shear and stable stratification (van Haren, 2008), convection in the preferential Ω-direction is, under non-linear stability, limited by a minimum stratification (and associated maximum near-inertial shear) to frequencies below $\sigma < f_h \approx 5$ f at the Challenger Deep. This limit-frequency is close to semidiurnal 2 Ω, as $f_h = 1.96$ Ω, besides lunar $M_2 = 1.93$ Ω, and the maximum IGW-bound $\sigma_{max} = 2.13$ Ω (for N = 2 f). The σ_{max} implies that, despite the rather weak large-scale stratification in N = 2 f < < 2 Ω, internal tides can freely propagate (in meridional but not latitudinal direction) as gravity waves as long as $M_2 < (N^2 + f_s^2)^{1/2}$ (LeBlond and Mysak, 1978). Their potential overturning after non-linear interactions may cause the short-scale spurs in the direction of Earth rotation, presumably following interaction with small-scale (near-inertial) shear.

Although the large-scale stratification in N ≥ 5 f reaches from the ocean-surface down to about 6 km at the top of the trench (van

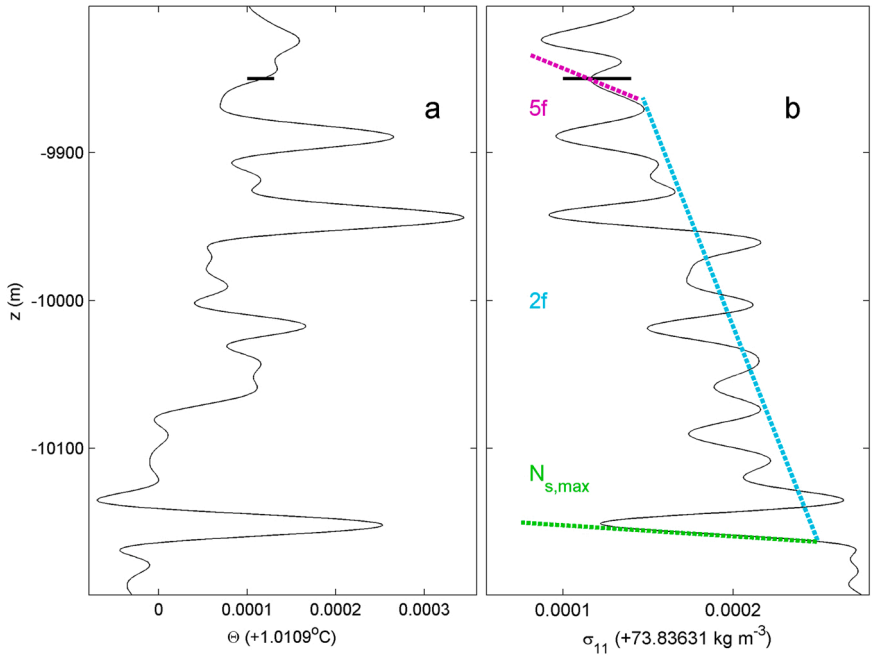

Fig. 10. Dz = 400-m detail of corrected CTD-profile from 2016 showing several relatively low-density spurs in 50-m low-pass filtered data. Error bars are given in black. (a) Conservative Temperature. (b) Density anomaly relative to 1.1×10^4 dbar. The coloured slopes relate to three buoyancy frequencies.

Haren et al., 2017), it is unlikely influencing the local short-scale turbulence spurs other than driving the internal tides and near-inertial motions (into the trench, following transformation from gravity to gyroscopic waves). Gyroscopic waves are internal waves in waters where $N = 0$ in which gravity cannot act as restoring force, and thus have the Coriolis force as the sole restoring force. The spurs are, on average, generated locally about 300 m higher-up, considering their heat (and salt) content and $N = 2$ f. The local patches have gradients that extend over about 25 m vertically, following small-scale $N_s = 5$ f, as observed (Fig. 10). If we interpret the warm anomalous spurs as the result of sparse breaking event (from somewhere above), their pathways do follow the direction of slantwise convection and their mean and maximum small-scale buoyancy frequencies are 5 f and 10 f, respectively. Hence, they reflect 3D non-linear and 1D linear stability, respectively (van Haren, 2008). Initial acceleration should overcome reduced gravity via downward velocity O(0.01) m s^{-1} over < 1 h (van Haren and Dijkstra, 2021). As much as vertical convection is halted by non-zero stratification, planetary slantwise convection is, without additional shear, halted by sufficient stratification in the Ω-direction, when locally $N > f_h$ (or 2 f_h).

As deep-sea internal wave breaking is a sporadic episodic event, with a puff here and a puff there, and given the slanting at different angles of shear generation and convection into the direction of Earth rotation, the spurs are presumably locally generated but, of course, not exactly vertically descending given their acute angles. As estimated by van Haren (2020) the small patches have horizontal sizes of about 40–75 m while an entire range of patches may occupy about 300–400 m vertically and horizontally. This explains their 'sudden' appearance in the near-vertical one-dimensional (1D)-instrumented line. In the direction of gravity however they are unstable, presumably especially under the (downward) acceleration by internal wave (breaking), such that $N = 2$ f can also not be sustained if sufficient destabilization would be available, e.g., under locally enhanced shear that overturns internal waves near $N_{s,max}$. Without sufficient shear, such weak stratification may exist and be maintained by a balance between advection and buoyancy fluxes due to geothermal heating from below and internal wave-induced turbulent diffusion from above.

4.2. What determines 'background' $N = 2$ f?

Besides IGW-breaking, geothermal heating is the only persistent candidate to destabilize stratification and provide buoyancy increase, which is to be balanced by advection. If one assumes a stable background with $N = 5$ f (as observed near the top of the trench) to be reduced to 2 f (in the trench), the buoyancy increase involves a stratification-equivalent of 3 f over a vertical range of about 5000 m. Throughout this range, the vertical turbulent flux contributing to buoyancy increase amounts $K_zN^2 = 6 \times 10^{-3}(2\,f)^2 = 2.1 \times 10^{-11}$ m^2 s^{-3} using the overall value for K_z in van Haren et al. (2021). The relatively low geothermal heating of $Q = 0.025$ W m^{-2} (Uyeda and Horai, 1979) provides an increase in buoyancy with time per unit length of $g\alpha_\theta Q/\rho c_p = 1.5 \times 10^{-11}$ m^2 s^{-3} in which g denotes the acceleration of gravity, $\alpha_\theta = 2.6 \times 10^{-4}$ °C^{-1} the thermal expansion coefficient, ρ the density and $c_p = 3980$ J kg^{-1} °C^{-1} the heat capacity of seawater. Hence, local internal wave-induced mixing and geothermal heating are expected to contribute about equally in reducing the stratification. In the above, horizontal advection is not considered, but if important it is expected to contribute to stability via the inflow of deep dense water masses. Geothermal heating is not directly observed in convection tubes of alternating warmer and colder water by the sensitive moored T-sensors, because the remaining stable stratification is too strong, even at $N = 2$ f.

4.3. Turbulent mixing reaching the trench floor

The short-scale spurs dominate turbulence in the deep trench, but mainly some distance above the trench floor. Occasionally, spurs do reach the trench floor, but unlike frictional shear motions, they are not expected to be capable of resuspending benthic materials, like geothermal convection. Once such matter has been resuspended by other turbulence processes such as flow-friction or, more likely above sloping topography, breaking internal waves, the convection turbulence induced by the slanted spurs may contribute to the transport of the suspended matter.

The (semi-)diurnal variations in deep-trench turbulence values are observed at some distance above the trench floor under depressed breaking near-inertial waves and, importantly, regularly reaching the trench floor. In the latter case, a distinct direct coupling existed with the passage of an atmospheric tropical storm passing just poleward of the Challenger Deep. During the 2.5-day (about one inertial period) passage the semidiurnal turbulence variations monotonically increased in amplitude, which was abruptly halted after the disappearance of the storm. The effect is an inertial period of semidiurnal-periodic largest turbulence observed near the trench floor in the one year record outside short-scale spur-peaks, and which reaches up to 200 m above the trench floor. Presumably the surface gradient barotropically sets up near-inertial motions in the deep, of which shear interacts with and modifies the internal tides into breaking.

4.4. Perspectives

Future research may focus on the 3D aspects of turbulence in general and the propagation and generation of short-scale spurs in particular. While 3D-sampling is difficult in shallow seas, it is a formidable task in the deep-ocean, notably deep trenches. Yet, from the perspective of learning about the characters and types of deep-trench turbulent mixing such effort may be worthwhile. Preferably, electronics of future temperature sensors should be made more stable and reduced in noise to achieve precision of < 0.00001 °C for extended resolution of turbulence subranges in deep-trench waters. Results may then be portable to modeling of deep-trench transport and redistribution of matter.

It would be good to combine physical oceanographic observations with multidisciplinary efforts, including simultaneous marine

geological measurements of heat flow, and marine chemical and biological observations to establish nutrient fluxes to verify carbon budgets.

5. Conclusions

-The deep-trench moored observations provide turbulence values that are to within error equivalent to those previously found by shipborne CTD. The mean turbulence dissipation rate of about 6×10^{-11} m^2 s^{-3} is an order of magnitude larger than in the open-ocean near the top of the trench.

-Short-scale spurs dominate turbulence values. The spurs are visible in the weak, but non-zero stratification and adopt slantwise pathways. The low level of shear in the trench allows the existence of low stratification that is unstable in the sense of planetary convection. The spurs are observed down to the level of small-scale locally stable stratification.

-The spurs are assumed to result from sparse internal wave breaking some 200–300 m higher-up, during the wave's downward phase.

-The internal (tidal) wave breaking may be initiated by near-inertial shear.

-Spectral analysis demonstrates dominant convection rather than shear near the trench floor. As spurs contribute less to turbulence near the trench floor, such convection is attributed to internal tidal wave breaking.

-During one observed event, local enhancement of internal tidal wave breaking was immediately observed in response to a passing tropical storm.

Declaration of Competing Interest

The author declares that he has no known competing financial interests or personal relationships that could have appeared to influence the work reported in this paper.

Data Availability

Data will be made available on request.

Acknowledgements

I thank the masters and crews of the R/V Sonne and R/V Sally Ride for the pleasant cooperation during the operations at sea. Atmospheric data were obtained from Meteoblue (https://www.meteoblue.com/) after payment. NIOZ temperature sensors have been partially supported by NWO, the Netherlands Organization for the advancement of science.

References

Bogorov, V.G., Kreps, E.M., 1958. To the question of the possibility of disposal of radioactive waste in deep-sea depressions of the ocean. Priroda 9, 45–50.
Bolgiano, R., 1959. Turbulent spectra in a stably stratified atmosphere. J. Geophys. Res. 64, 2226–2229.
Dalziel, S.B., Patterson, M.D., Caulfield, C.P., Coomaraswamy, I.A., 2008. Mixing efficiency in high-aspect-ratio Rayleigh-Taylor experiments. Phys. Fluids 20, 065106.
Dillon, T.M., 1982. Vertical overturns: a comparison of Thorpe and Ozmidov length scales. J. Geophys. Res 87, 9601–9613.
Eriksen, C.C., 1982. Observations of internal wave reflection off sloping bottoms. J. Geophys. Res. 87, 525–538.
Galbraith, P.S., Kelley, D.E., 1996. Identifying overturns in CTD profiles. J. Atmos. Ocean. Technol. 13, 688–702.
Gallo, N.D., Cameron, J., Hardy, K., Fryer, P., Bartlett, D.H., Levin, L.A., 2015. Submersible- and lander-observed community patterns in the Mariana and New Britain trenches: influence of productivity and depth on epibenthic and scavenging communities. Deep-Sea Res. I 99, 119–133.
Gerkema, T., 2019. An Introduction To Tides. Cambridge University Press,, Cambridge, UK.
Glud, R.N., et al., 2013. High rates of microbial carbon turnover in sediments in the deepest oceanic trench on Earth. Nat. Geosci. 6, 284–288.
Gregg, M.C., D'Asaro, E.A., Riley, J.J., Kunze, E., 2018. Mixing efficiency in the ocean. Ann. Rev. Mar. Sci. 10, 443–473.
Huber, K., 2018. Analog sampling: what do accuracy, sensitivity, precision, and noise mean? ⟨https://www.embedded.com/analog-sampling-what-do-accuracy-sensitivity-precision-and-noise-mean/⟩, accessed 26 April 2023.
IOC, SCOR, IAPSO, 2010. The international thermodynamic equation of seawater – 2010: Calculation and use of thermodynamic properties, Intergovernmental Oceanographic Commission, Manuals and Guides No. 56, UNESCO, Paris F.
Jamieson, A., 2015. The hadal zone, life in the deepest oceans. Cambridge University Press,, Cambridge, UK.
Jayne, S.R., St. Laurent, L.C., 2001. Parameterizing tidal dissipation over rough topography. Geophys. Res. Lett. 28, 811–814.
Kueh, M.-T., et al., 2019. Effects of horizontal resolution and air–sea flux parameterization on the intensity and structure of simulated Typhoon Haiyan (2013). Nat. Hazards Earth Sys. Sci. 19, 1509–1539.
LeBlond, P.H., Mysak, L.A., 1978. Waves in the Ocean. Elsevier,, Amsterdam, NL.
Mater, B.D., Venayagamoorthy, S.K., St. Laurent, L., Moum, J.N., 2015. Biases in Thorpe scale estimation of turbulence dissipation. Part I: assessments from large-scale overturns in oceanographic data. J. Phys. Oceanogr. 45, 2497–2521.
Morozov, E.G., Velarde, M.G., 2008. Inertial oscillations as deep ocean response to hurricanes. J. Oceanogr. 64, 495–509.
Nash, J.D., Alford, M.H., Kunze, E., Martini, K., Kelly, S., 2007. Hotspots of deep ocean mixing on the Oregon. Geophys. Res. Lett. 34, L01605 https://doi.org/10.1029/2006GL028170.
Nunoura, T., et al., 2015. Hadal biosphere: Insight into the microbial ecosystem in the deepest ocean on Earth. Proc. Nat. Ac. Sci. 112, E1230–E1236.
Oakey, N.S., 1982. Determination of the rate of dissipation of turbulent energy from simultaneous temperature and velocity shear microstructure measurements. J. Phys. Oceanogr. 12, 256–271.
Osborn, T.R., 1980. Estimates of the local rate of vertical diffusion from dissipation measurements. J. Phys. Oceanogr. 10, 83–89.
Parks, T.W., Burrus, C.S., 1987. Digital Filter Design. Wiley,, New York, USA.

Pawar, S.S., Arakeri, J.H., 2016. Kinetic energy and scalar spectra in high Rayleigh number axially homogeneous buoyancy driven turbulence. Phys. Fluids 28, 065103.
Portwood, G.D., de Bruyn Kops, S.M., Caulfield, C.P., 2019. Asymptotic dynamics of high dynamic range stratified turbulence. Phys. Rev. Lett. 122, 194504.
Ravens, T.M., Kocsis, O., Wüest, A., Granin, N., 2000. Small-scale turbulence and vertical mixing in Lake Baikal. Limnol. Oceanogr. 45, 159–173.
Sarkar, S., Scotti, A., 2017. From topographic internal gravity waves to turbulence. Ann. Rev. Fluid Mech. 49, 195–220.
Shay, L.K., Elsberry, R.L., 1987. Near-inertial ocean current response to hurricane Frederic. J. Phys. Oceanogr. 17, 1249–1269.
Sheremet, V.A., 2004. Laboratory experiments with tilted convective plumes on a centrifuge: a finite angle between the buoyancy and the axis of rotation. J. Fluid Mech. 506, 217–244.
Straneo, F., Kawase, M., Riser, S.C., 2002. Idealized models of slantwise convection in a baroclinic flow. J. Phys. Oceanogr. 32, 558–572.
Taira, K., Kitagawa, S., Yamashiro, T., Yanagimoto, D., 2004. Deep and bottom currents in the Challenger Deep, Mariana Trench, measured with super-deep current meters. J. Oceanogr. 60, 919–926.
Taira, K., Yanagimoto, D., Kitagawa, S., 2005. Deep CTD casts in the Challenger Deep. Mariana Trench. J. Oceanogr. 61, 447–454.
Tareev, B.A., 1959. Free convection in deep depressions of the ocean. Rep. Acad. Sci. USSR 127 (5), 1005–1008.
Tennekes, H., Lumley, J.L., 1972. A First in Turbulence. MIT Press,, Boston, MA, USA.
Thorpe, S.A., 1977. Turbulence and mixing in a Scottish loch. Philos. Trans. Roy. Soc. Lond. A 286, 125–181.
Thorpe, S.A., 1987. Transitional phenomena and the development of turbulence in stratified fluids: a review. J. Geophys. Res. 92, 5231–5248.
Uyeda, S., 1984. Subduction zones: their diversity, mechanism and human impacts. GeoJ 8, 381–406.
Uyeda, S., Horai, K., 1979. Heat flow measurements on deep sea drilling project leg 60. Initial Rep. Deep Sea Drill. Proj. 60, 789–800. https://doi.org/10.2973/dsdp.proc.60.146.1982.
van Haren, H., 2008. Abrupt transitions between gyroscopic and internal gravity waves: the mid-latitude case. J. Fluid Mech. 598, 67–80.
van Haren, H., 2018. Philosophy and application of high-resolution temperature sensors for stratified waters. Sensors 18, 3184. https://doi.org/10.3390/s18103184.
van Haren, H., 2020. Challenger deep internal wave turbulence events. Deep-Sea Res. I 165, 103400.
van Haren, H., 2022. Thermistor string corrections in data from very weakly stratified deep-ocean waters. Deep-Sea Res. I 189, 103870.
van Haren, H., Dijkstra, H.A., 2021. Convection under internal waves in an alpine lake. Env. Fluid Mech. 21, 305–316.
van Haren, H., Berndt, C., Klaucke, I., 2017. Ocean mixing in deep-sea trenches: new insights from the challenger deep. Marian. Trench Deep-Sea Res. I 129, 1–9.
van Haren, H., Chi, W.-C., Yang, C.-F., Yang, Y.J., Jan, S., 2020. Deep sea floor observations of typhoon driven enhanced ocean turbulence. Progr. Oceano 184, 102315.
van Haren, H., Uchida, H., Yanagimoto, D., 2021. Further correcting pressure effects on SBE911 CTD-conductivity data from hadal depths. J. Oceanogr. 77, 137–144.
Warhaft, Z., 2000. Passive scalars in turbulent flows. Ann. Rev. Fl. Mech. 32, 203–240.
Wirth, A., Barnier, B., 2006. Tilted convective plumes in numerical experiments. Ocean Modell. 12, 101–111.